Coherent Control of Spin in Color Centers in Wide-Bandgap Semiconductors

in collaboration with
the National University of Singapore

THESIS

submitted in partial fulfillment of the
requirements for the degree of

MASTER OF SCIENCE
in
PHYSICS

Author :	Oscar Ociepka
Student ID :	s2669684
Supervisor (Leiden) :	Dr.ir. B.J. Hensen
Supervisor (Singapore) :	Dr. A.A. Bettiol

Singapore, December 22, 2025

Coherent Control of Spin in Color Centers in Wide-Bandgap Semiconductors

Oscar Ociepka

Huygens-Kamerlingh Onnes Laboratory, Leiden University
P.O. Box 9500, 2300 RA Leiden, The Netherlands

December 22, 2025

Abstract

Color centers in wide-bandgap semiconductors provide a promising platform for room-temperature quantum technologies due to their optical addressability and long-lived spin states. In this thesis, optical and spin properties of defect centers are investigated in two material systems: hexagonal boron nitride and pink diamond. Photoluminescence spectroscopy is used to characterize emission features of multiple hBN flakes under different excitation wavelengths and following helium implantation, revealing reproducible spectral features but no clear implantation-induced modifications. In parallel, optically detected magnetic resonance and time-domain measurements are performed on nitrogen-vacancy centers in pink diamond, demonstrating coherent spin control through Rabi oscillations. From these measurements, a transverse spin coherence time of $T_2 = (0.65 \pm 0.22)\ \mu$s is extracted. While the results do not allow definitive identification of all defect species or relaxation mechanisms, this work establishes a consistent experimental and analytical framework for future studies of color centers in wide-bandgap semiconductors at ambient conditions.

Contents

Chapter 1

Introduction

Over the past decades, quantum mechanics has evolved from a purely foundational theory into the backbone of emerging technologies. Quantum information science, encompassing quantum computation, communication, and sensing, promises capabilities that fundamentally surpass those of classical systems, including exponential speedups, unconditionally secure communication, and ultrasensitive detection of fields and forces [1, 2]. Realizing these promises in practical devices, however, remains a major technological challenge. Many leading quantum platforms rely on cryogenic temperatures, ultra-high vacuum, or complex infrastructure, which limits scalability and imposes a significant energetic and environmental cost [3, 4]. Developing quantum systems that operate at or near ambient conditions would therefore not only simplify implementation, but also enable more sustainable and accessible quantum technologies.

Solid-state defect centers in wide-band gap semiconductors have emerged as particularly attractive candidates in this context. These atomic-scale defects host localized electronic states whose optical and spin properties can be coherently controlled, often even at room temperature [5, 6]. Among their most remarkable features are long spin coherence times, bright photoluminescence, and the possibility of optical initialization and readout, making them suitable for applications ranging from quantum memories to nanoscale magnetometry [7]. Crucially, their solid-state nature allows integration with existing semiconductor and photonic platforms, offering a clear pathway toward scalable devices.

A well-known example of such a system is the nitrogen-vacancy center, or color center, in diamond, which has been extensively studied for

its exceptional spin coherence and robustness under ambient conditions [8]. Beyond diamond, a growing body of research has focused on alternative host materials, motivated by the search for new defect species with improved optical stability, tunable emission wavelengths, or enhanced coherence properties [9]. Wide-band gap materials such as silicon carbide and hexagonal boron nitride have attracted particular interest, as they combine strong optical transitions with material platforms that are compatible with large-scale fabrication [10, 11].

A central goal in the study of color centers is the characterization of their optical and spin properties. Photoluminescence spectroscopy provides insight into the electronic structure of defect states through zero-phonon lines and phonon sidebands, while optically detected magnetic resonance enables direct access to spin transitions and coherence properties. Key figures of merit include the spin relaxation time T_1 and the spin coherence time T_2, which determine the suitability of a given defect for coherent control and sensing applications.

Hexagonal boron nitride is another material that has attracted significant attention as a host material for quantum emitters [12]. As a layered van der Waals crystal with a large band gap, hBN can support bright and stable single-photon emission at room temperature. These defects can exhibit narrow zero-phonon lines, high brightness, and in some cases single-photon emission at room temperature [13–15]. Despite intense experimental and theoretical effort, the microscopic origin of many observed emission lines in hexagonal boron nitride remains under debate, and reported photoluminescence spectra often vary strongly between samples and fabrication methods [16]. Careful spectroscopic characterization is therefore essential to relate observed optical features to specific defect configurations.

In parallel, color centers in diamond with emission in the visible and near-infrared range continue to serve as a benchmark system for coherent spin control. Optically detected magnetic resonance allows direct access to spin transitions, enabling the measurement of coherence times and the implementation of pulsed control protocols such as Rabi oscillations and spin-echo sequences [17]. These techniques provide a powerful framework for assessing the suitability of a given defect system for quantum information and sensing applications.

In this thesis, coherent spin control and optical characterization of color

centers in wide-band gap semiconductors are investigated using a combination of photoluminescence spectroscopy and optically detected magnetic resonance. Two material systems are studied in parallel. The first part focuses on photoluminescence measurements of defect centers in hexagonal boron nitride flakes, with the aim of identifying and contextualizing observed emission features. The second part investigates spin coherence in pink diamond through optically detected magnetic resonance and time-domain measurements, including Rabi oscillations and coherence-time extraction. While the available data do not allow for definitive identification of all defect species or relaxation mechanisms, the results provide insight into the experimental limitations, reproducibility, and prospects of these systems for room-temperature quantum technologies.

1.1 Structure

Chapter 2 introduces the theoretical background relevant to this work, covering the basic principles of optical defects in wide-band gap semiconductors, photoluminescence processes, and coherent spin control as accessed through optically detected magnetic resonance. Chapter 3 describes the experimental methods and setups used throughout the project, including optical spectroscopy and microwave control techniques.

The experimental results are presented in Chapter 4, which is divided into two main parts: photoluminescence measurements of defect centers in hexagonal boron nitride, and spin-resonance and coherence measurements performed on pink diamond. Chapter 5 discusses these results in the context of existing literature, addresses experimental limitations, and outlines possible directions for future work. The thesis concludes with a summary of the main findings and their implications for room-temperature quantum technologies.

Chapter 2

Theory

This chapter provides the theoretical background necessary to interpret the experimental results presented later in this thesis. The focus lies on the optical and spin-related properties of color centers in wide-band gap semiconductors, with particular emphasis on systems relevant to room-temperature quantum applications.

Section 2.1 introduces color centers as localized defects in crystalline hosts, discussing their electronic structure, optical transitions, and spin degrees of freedom. Section 2.2 focuses on optical spectroscopy of such defects, outlining the principles of photoluminescence, zero-phonon lines, and phonon sidebands, as well as the influence of excitation wavelength on observed spectra. In Section 2.3, the spin physics underlying optically detected magnetic resonance is developed, including the spin Hamiltonian, zero-field splitting, and the mechanism of optical spin readout. Finally, Section 2.4 discusses coherent spin control, covering driven spin dynamics, Rabi oscillations, and the physical meaning of the spin relaxation and decoherence times T_1 and T_2.

2.1 Color centers in wide-bandgap semiconductors

Solid-state color centers form a central platform for room-temperature quantum technologies. They combine the robustness and scalability of crystalline materials with atom-like electronic and spin properties, enabling coherent quantum control without the need for extreme experimental con-

ditions [5, 6]. In this section, the physical origin of color centers is introduced, starting from the electronic structure of semiconductors and progressing toward the lattice-scale defects that give rise to optically and magnetically addressable quantum states.

2.1.1 Semiconductors and band structure

In crystalline solids, the periodic arrangement of atoms gives rise to an electronic band structure. Within the independent-electron approximation, the allowed energy levels form continuous bands separated by forbidden energy regions known as bandgaps. The electronic properties of a solid are determined primarily by the occupancy of the valence band and conduction band.

A semiconductor is characterized by a finite bandgap E_g between the valence band maximum E_v and conduction band minimum E_c,

$$E_g = E_c - E_v. \tag{2.1}$$

At zero temperature, the valence band is filled and the conduction band is empty. At finite temperature, thermal excitation can promote electrons across the bandgap, generating mobile charge carriers. The intrinsic carrier concentration n_i scales approximately as

$$n_i \propto \exp\left(-\frac{E_g}{2k_B T}\right), \tag{2.2}$$

where k_B is the Boltzmann constant and T the temperature. As a result, materials with larger bandgaps exhibit significantly reduced thermal carrier densities at room temperature.

2.1.2 Wide-bandgap semiconductors

Wide-bandgap semiconductors are defined as materials with bandgaps typically exceeding 2.5 eV. Prominent examples include diamond ($E_g \approx$ 5.5 eV), silicon carbide ($E_g \approx 3.2$ eV), and hexagonal boron nitride ($E_g \approx$ 6.0 eV) [9]. The large bandgap suppresses thermally activated charge carriers, leading to low electrical noise and enhanced stability of localized electronic states at ambient temperatures.

From the perspective of quantum information science, wide-bandgap materials are particularly attractive because they can host defect states

whose energy levels lie deep within the bandgap. These deep-level states are well isolated from the conduction and valence bands, reducing phonon-assisted ionization and enabling long spin lifetimes and coherence times even at room temperature [7].

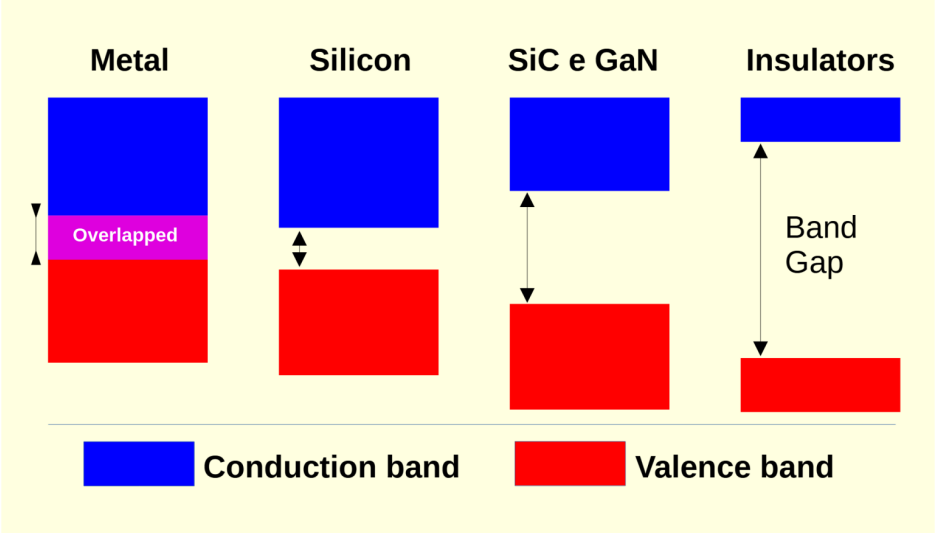

Figure 2.1: *Comparison of wide-bandgap semiconductor (SiC & GaN) energy bandgaps to metals, a conventional semiconductor (Silicon) and an insulator. Image retrieved [18].*

2.1.3 Color centers as point defects

A color center is a point defect in a crystal lattice that introduces localized electronic states within the bandgap. These defects can arise from vacancies, substitutional impurities, or more complex defect complexes. The presence of such a defect modifies the local electrostatic potential, producing discrete energy levels that can participate in optical transitions.

Optical absorption or emission occurs when an electron transitions between defect levels, or between a defect level and a band edge. The emitted photon energy E_γ is given by

$$E_\gamma = E_i - E_f, \tag{2.3}$$

where E_i and E_f are the initial and final electronic energies of the defect state. If the transition occurs without phonon participation, the emission

appears as a zero-phonon line, while phonon-assisted processes produce sidebands.

2.1.4 Lattice structure and defect symmetry

The host lattice plays a crucial role in determining the electronic and spin properties of a color center. Diamond crystallizes in a cubic lattice with tetrahedral coordination, while hexagonal boron nitride forms a layered hexagonal structure composed of alternating boron and nitrogen atoms [8, 14]. The symmetry of the lattice constrains the allowed electronic orbitals and spin interactions of embedded defects.

For example, the nitrogen-vacancy centre in diamond consists of a substitutional nitrogen atom adjacent to a carbon vacancy. Its symmetry axis defines a quantization direction for the electronic spin, with there being four crystallographic orientations, seen in Figure 2.2. In contrast, defects in hexagonal boron nitride reside in a two-dimensional lattice with reduced symmetry, leading to a broader diversity of possible defect configurations and optical signatures [16].

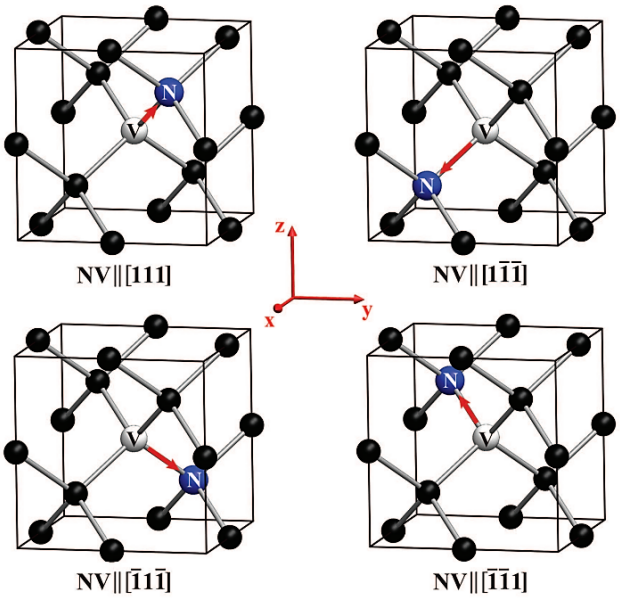

Figure 2.2: *Four possible crystallographic orientations of an NV in diamond. While these do not differ fundamentally, they will react differently to external couplings due to fixed axes. Image retrieved [19].*

2.1.5 Spin degrees of freedom in color centers

Many color centers possess unpaired electron spins, making them suitable for quantum manipulation. The electronic spin operator $\hat{\mathbf{S}}$ obeys standard angular momentum commutation relations, and in the presence of a magnetic field $\mathbf{B}$, the Zeeman interaction contributes a term to the Hamiltonian

$$\hat{H}_Z = g\mu_B \mathbf{B} \cdot \hat{\mathbf{S}}, \tag{2.4}$$

where g is the Landé g-factor and μ_B the Bohr magneton.

In addition to the Zeeman interaction, crystal-field effects can lift degeneracies even in the absence of an external field, producing zero-field splitting terms that are characteristic of a given defect. These spin properties form the foundation for optically detected magnetic resonance and coherent spin control, which are discussed in subsequent sections.

2.2 Optical spectroscopy of defects

Optical spectroscopy provides a primary tool for identifying and characterizing defect centers in wide-bandgap semiconductors. Photoluminescence measurements probe electronic transitions associated with localized defect states and reveal information about electron-phonon coupling and defect symmetry.

2.2.1 Photoluminescence

Photoluminescence occurs when a system absorbs photons and subsequently emits light following radiative relaxation. For a defect center, optical excitation promotes an electron from a ground electronic state $|g\rangle$ to an excited state $|e\rangle$. After relaxation, photon emission occurs with energy

$$E_{\mathrm{em}} = E_e - E_g - E_{\mathrm{ph}}, \tag{2.5}$$

where E_{ph} accounts for phonon participation.

The measured photoluminescence spectrum reflects the density of optical transitions weighted by their radiative probabilities. In practice, spectra often consist of sharp features superimposed on a broader background.

2.2.2 Nitrogen vacancy spin physics

The negatively charged nitrogen-vacancy (NV^-) center in diamond . Its electronic ground state is a spin triplet with total spin quantum number $S = 1$, giving rise to three spin sublevels $m_s = 0, \pm 1$ [8]. Even in the absence of an external magnetic field, these sublevels are split by the spin-spin interaction, described by the zero-field splitting parameter $D \approx 2.87$ GHz.

Optical excitation promotes electrons from the ground state to higher-lying excited states. These excited states relax rapidly into the optically excited triplet state, from which radiative decay back to the ground state occurs via the zero-phonon line and phonon sideband, as in Figure 2.3. During this optical cycling, spin-conserving transitions dominate, but non-radiative decay through intermediate singlet states occurs with a higher probability for the $m_s = \pm 1$ sublevels.

The spin-dependent intersystem crossing leads to two key effects: first, the photoluminescence intensity associated with the $m_s = 0$ state is higher than that of the $m_s = \pm 1$ states, enabling optical spin readout; second, continuous optical excitation preferentially pumps population into the $m_s = 0$ ground state, providing a mechanism for optical spin initialization [17]. These properties form the basis for optically detected magnetic resonance and coherent spin control in diamond.

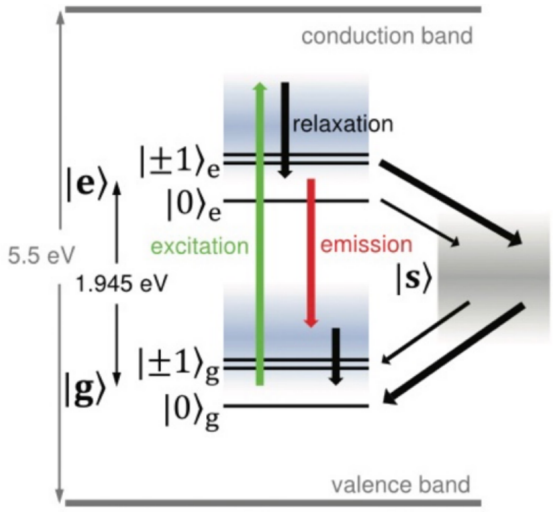

Figure 2.3: *Band structure of spin dynamics in a nitrogen vacancy center in diamond. Image retrieved [20].*

2.2.3 Zero-phonon lines and phonon sidebands

The zero-phonon line corresponds to a purely electronic transition without phonon involvement. Its energy directly reflects the electronic level spacing of the defect:

$$E_{\mathrm{ZPL}} = E_e - E_g. \tag{2.6}$$

Electron-phonon coupling gives rise to phonon sidebands at lower energies. The relative intensity of the ZPL is commonly quantified by the Debye-Waller factor

$$\mathrm{DW} = \frac{I_{\mathrm{ZPL}}}{I_{\mathrm{total}}}, \tag{2.7}$$

where I_{total} is the integrated emission intensity. Strong phonon coupling, common in hBN, leads to reduced ZPL visibility [14]. A visualization of the ZPL and PSB in diamond NV can be seen in Figure 2.4.

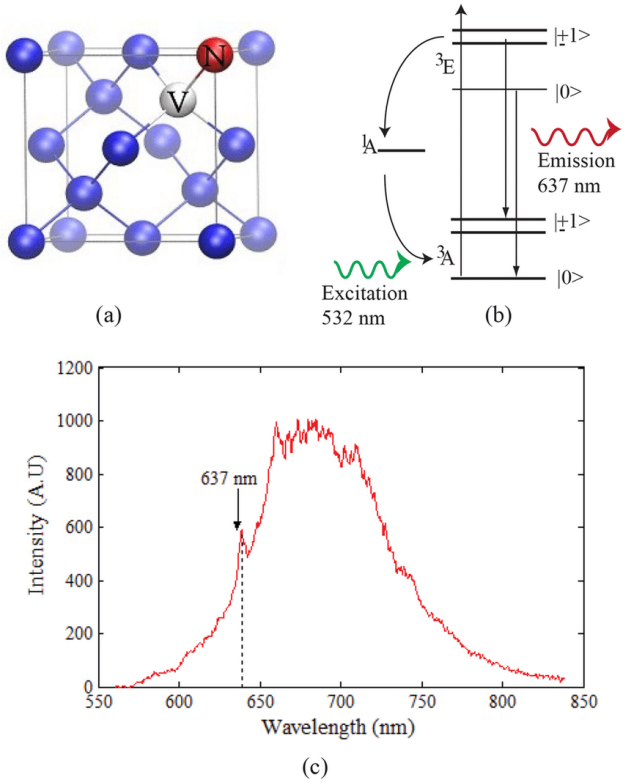

Figure 2.4: *(a) Diamond NV in a lattice; (b) Corresponding band structure; (c) PL spectrum of the ZPL at 637 nm and the PSB to its right. Image retrieved [21].*

2.2.4 Dependence on excitation wavelength

The observed PL spectrum can depend strongly on the excitation wavelength. Different excitation energies may preferentially address distinct defect species, charge states, or excitation pathways. For example, excitation at 405 nm and 532 nm probes different regions of the absorption spectrum and may yield qualitatively different emission features in heterogeneous samples.

Such wavelength dependence complicates defect identification but also provides an additional diagnostic tool for distinguishing between competing emission mechanisms [11, 15].

2.3 Optically detected magnetic resonance

Optically detected magnetic resonance (ODMR) enables the manipulation and detection of spin states through a combination of optical and microwave fields.

2.3.1 Ground-state spin Hamiltonian

The effective ground-state spin Hamiltonian of a color center with electronic spin $\mathbf{S}$ can be written as

$$\hat{H} = \hat{H}_{\mathrm{ZFS}} + \hat{H}_{\mathrm{Z}} + \hat{H}_{\mathrm{hf}}, \tag{2.8}$$

where $\hat{H}_{\mathrm{ZFS}}$ describes zero-field splitting, $\hat{H}_{\mathrm{Z}}$ is the Zeeman interaction with an external magnetic field, and $\hat{H}_{\mathrm{hf}}$ accounts for hyperfine coupling to nearby nuclear spins [17].

2.3.2 Zero-field splitting

Zero-field splitting arises from spin-spin interactions in systems with total electronic spin $S \geq 1$, and reflects anisotropies in the local crystal field experienced by the defect. Even in the absence of an external magnetic field, these interactions lift the degeneracy between spin sublevels and define an intrinsic energy scale of the spin system.

For an axially symmetric defect, the zero-field splitting contribution to the spin Hamiltonian is commonly written as

$$\hat{H}_{\mathrm{ZFS}} = D\left(S_z^2 - \frac{S(S+1)}{3}\right), \tag{2.9}$$

where D is the zero-field splitting parameter, S is the total electronic spin quantum number, and S_z is the spin projection operator along the symmetry axis of the defect. The subtraction of $S(S+1)/3$ ensures that the Hamiltonian is traceless and does not shift the overall energy reference.

Physically, the parameter D quantifies the strength of the internal spin-spin interaction and depends on the electronic wavefunction and local lattice environment of the defect. For the nitrogen-vacancy center in diamond, which has $S = 1$, this term splits the $m_S = 0$ and $m_S = \pm 1$ sublevels by an energy $D \approx 2.87$ GHz at zero magnetic field [8]. This intrinsic splitting forms the basis for optically detected magnetic resonance and coherent spin manipulation.

2.3.3 ODMR principle

In ODMR, resonant microwave radiation drives transitions between spin sublevels. These transitions modify the photoluminescence intensity due to spin-dependent optical cycling. By sweeping the microwave frequency and monitoring the PL signal, spin resonances can be detected optically.

The ODMR contrast depends on the efficiency of spin polarization, the strength of the microwave driving field, and the relaxation dynamics of the system.

2.4 Coherent spin control

Time-domain microwave control enables coherent manipulation of spin states and provides access to intrinsic relaxation and decoherence processes.

2.4.1 Rabi oscillations

The interaction between the electronic spin and an applied microwave magnetic field can be described by a time-dependent driving Hamiltonian

of the form

$$\hat{H}_{\text{drive}} = \gamma B_1 \cos(2\pi\nu t)\, \hat{S}_x, \tag{2.10}$$

where γ is the gyromagnetic ratio, B_1 the microwave field amplitude, ν the driving frequency, and $\hat{S}_x$ the spin operator along the field direction.

Under resonant driving with angular frequency ω, the spin undergoes coherent oscillations between two levels. The probability of occupying the excited state evolves as

$$P(t) = \sin^2\left(\frac{\Omega_R t}{2}\right), \tag{2.11}$$

where $\Omega_R = \gamma B_1$ is the Rabi frequency, proportional to the microwave field amplitude.

In real systems, these oscillations are damped due to decoherence:

$$P(t) = \sin^2\left(\frac{\Omega_R t}{2}\right) \exp\left(-\frac{t}{T_2}\right). \tag{2.12}$$

2.4.2 Spin relaxation time T_1

The longitudinal relaxation time T_1 characterizes the return of the spin population to thermal equilibrium along the quantization axis. Physically, it describes the timescale over which energy is exchanged between the spin system and its environment, often referred to as the spin lattice. It is defined through the recovery of the longitudinal magnetization,

$$M_z(t) = M_z(0) + [M_z(\infty) - M_z(0)]\left(1 - e^{-t/T_1}\right), \tag{2.13}$$

where $M_z(t)$ is the expectation value of the spin projection along the quantization axis at time t, $M_z(0)$ is the initial polarization, and $M_z(\infty)$ denotes the equilibrium polarization.

The T_1 process involves transitions between spin energy levels and therefore requires mechanisms that can absorb or supply the corresponding energy. In solid-state systems, this energy exchange is typically mediated by lattice phonons whose energies match the spin splitting. As a result, T_1 is strongly influenced by temperature, lattice vibrations, and the phonon density of states of the host material.

Long T_1 times indicate weak coupling between the spin and its environment and are desirable for quantum applications, as they set an upper bound on how long a spin state can be preserved before thermalization. Although T_1 does not directly limit phase coherence, it ultimately constrains the maximum achievable coherence time and the repetition rate of spin-based experiments.

2.4.3 Spin coherence time T_2

The transverse coherence time T_2 quantifies the decay of phase coherence between quantum superposition states. Unlike T_1, which concerns population relaxation, T_2 describes how long a well-defined relative phase between spin states is maintained. This coherence is encoded in the off-diagonal elements of the spin density matrix, which decay according to

$$\rho_{01}(t) = \rho_{01}(0) \exp\left(-\frac{t}{T_2}\right), \tag{2.14}$$

where $\rho_{01}(t)$ represents the coherence between two spin levels at time t.

The decay of coherence arises from two distinct processes. The first is energy relaxation, which is directly related to T_1, and the second is pure dephasing caused by fluctuations in the local magnetic or electric environment. These fluctuations lead to random phase accumulation between spins, even in the absence of energy exchange. The combined effect is captured by the relation

$$\frac{1}{T_2} = \frac{1}{2T_1} + \frac{1}{T_\phi}, \tag{2.15}$$

where T_ϕ denotes the pure dephasing time associated with environmental noise.

In practice, T_2 is the most relevant timescale for coherent control experiments such as Rabi oscillations and spin echo measurements. It determines the maximum duration over which microwave-driven spin manipulation can be performed reliably. For quantum information processing and sensing applications, long T_2 times are essential, as they directly set the window for coherent operations and high-fidelity readout [7].

Chapter 3

Methods

This chapter describes the experimental methods used to prepare, characterize, and measure color centers in wide-bandgap semiconductor samples. It outlines the sample systems studied, the optical and microwave instrumentation employed, and the measurement protocols used to acquire photoluminescence and spin-resonance data.

Section 3.1 introduces the investigated samples, being hexagonal boron nitride flakes on silicon substrates and helium-implanted pink diamond, and discusses the fabrication and ion-implantation processes relevant to this work. Section 3.2 presents the combined optical and microwave experimental setup used for photoluminescence spectroscopy, optically detected magnetic resonance, and coherent spin control, including laser excitation, detection optics, microwave delivery, and control electronics. Measurement protocols are detailed in Section 3.3, covering photoluminescence spectroscopy, continuous-wave ODMR, pulsed microwave measurements, and the experimental procedure for measuring the spin relaxation time T_1, though this was not performed. Finally, Section 3.4 summarizes the data analysis methods used to process spectra and time-domain measurements, including fitting procedures and parameter extraction.

3.1 Samples and ion implantation

Two solid-state samples were investigated in this work: a pink diamond containing nitrogen-vacancy centers, and a silicon substrate supporting carbon-sputtered hexagonal boron nitride flakes. Both samples are based on wide-bandgap host materials and were selected for their relevance to

room-temperature color center studies.

3.1.1 Pink diamond

The pink diamond sample, called so for its pink appearance under the correct lighting (see Figure 3.1), was a chemical vapor deposition (CVD) grown single-crystal diamond with dimensions of approximately 5 mm $\times$ 5 mm. This sample is identical to one studied in previous work[22] and contains a native ensemble of nitrogen-vacancy centers formed during growth. All optically detected magnetic resonance and coherent spin control measurements presented in this thesis were performed on the diamond prior to any additional processing.

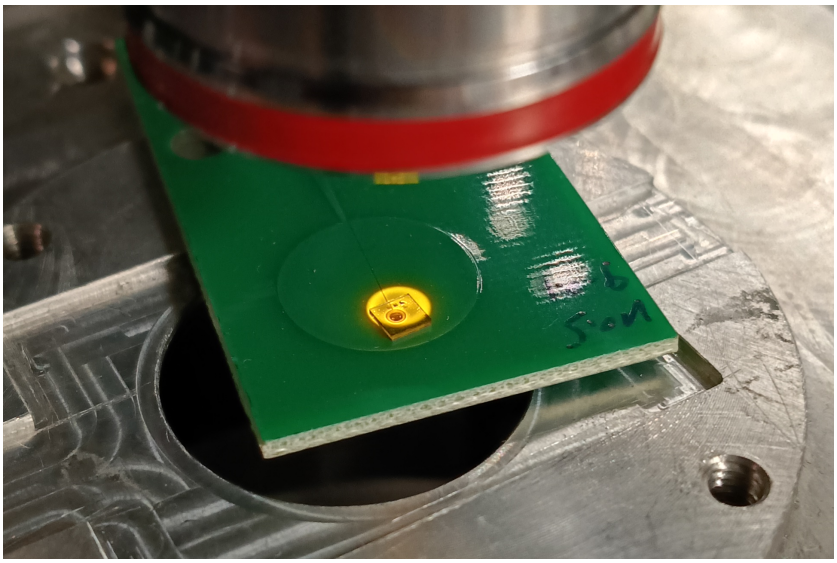

Figure 3.1: *Photo of the pink diamond sample in position under the microscope, illuminated by polychromatic light.*

After the measurements reported in the Results chapter, the diamond was implanted with helium ions at the Centre for Ion Beam Applications (CIBA) in Singapore. The implantation was performed using 500 keV He^+ ions in six square regions of 500 μm $\times$ 500 μm, each exposed to a different ion fluence ranging from 1×10^{14} to 3×10^{16} ions/cm^2, equally spaced, as shown in Figures 3.2 and 3.3. Although no post-implantation results are included in this work, the procedure is mentioned for completeness and relevance to future studies on defect engineering in diamond.

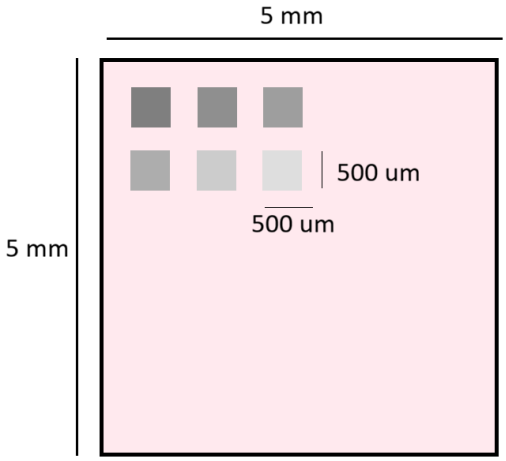

Figure 3.2: *Schematic of the six 500 keV He^+ implantation areas within the pink diamond sample. From high dosage (dark gray) to low dosage (light gray): 3e16, 1e16, 3e15, 1e15, 3e14, 1e14 ions per square centimeter.*

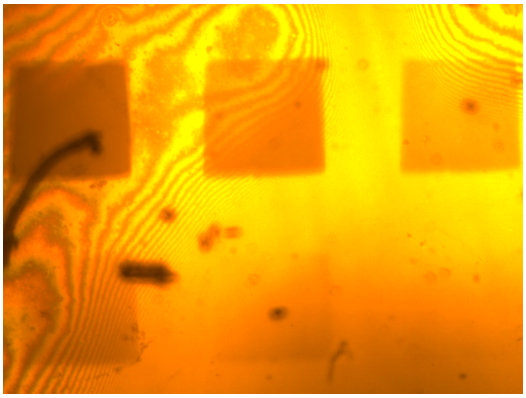

Figure 3.3: *The six He^+ implantation areas as viewed under an optical microscope. It is immediately apparent that the high dosage areas are darker, and consequently, varying photoluminescent behavior can be reasonably expected.*

3.1.2 Hexagonal boron nitride

The second sample consisted of hexagonal boron nitride flakes supported on a silicon substrate, with an additional carbon layer deposited by sputtering prior to ion implantation. The precise method used to transfer the hBN flakes onto the silicon substrate, as well as the parameters of the carbon sputtering process, were not part of this project and are therefore not discussed in detail. The sample was implanted uniformly with helium ions at CIBA, although the exact implantation dose is unknown.

3.1.3 Particle accelerator

Ion implantation was carried out at CIBA using a particle accelerator, which generates and accelerates ions to well-defined kinetic energies using electric fields. The ions penetrate the target material and lose energy through collisions with lattice atoms, creating vacancies and defect complexes along their trajectories. In wide-bandgap materials, such implantation-induced defects can modify the optical and spin properties of existing color centers or contribute to the formation of new ones. The controlled introduction of lattice damage via ion implantation is therefore a widely used technique for tailoring defect densities in quantum materials.

3.2 Experimental setup

All optical and spin-resonance measurements in this work were performed using a room-temperature confocal microscope platform integrated with microwave delivery and electronic control. The setup is designed to enable spatially resolved photoluminescence spectroscopy as well as optically detected magnetic resonance measurements on solid-state defect centers. While individual experimental protocols varied between measurements, the underlying hardware configuration remained largely unchanged throughout the project.

The experimental system is conceptually similar to that used in previous work on diamond color centers and wide-bandgap materials, and is optimized for flexibility rather than single-purpose performance. In the following, the main components of the optical microscope, microwave delivery chain, and integrated ODMR configuration are described.

3.2.1 Confocal optical microscope

All measurements were carried out on a home-built confocal microscope based on a Zeiss Examiner Z1 platform. The microscope provides a mechanically stable frame and precise digital positioning, enabling optical access to micron-scale regions of interest within the samples. Samples were mounted on a motorized piezoelectric stage, allowing raster scanning for spatial mapping and accurate repositioning during repeated measurements.

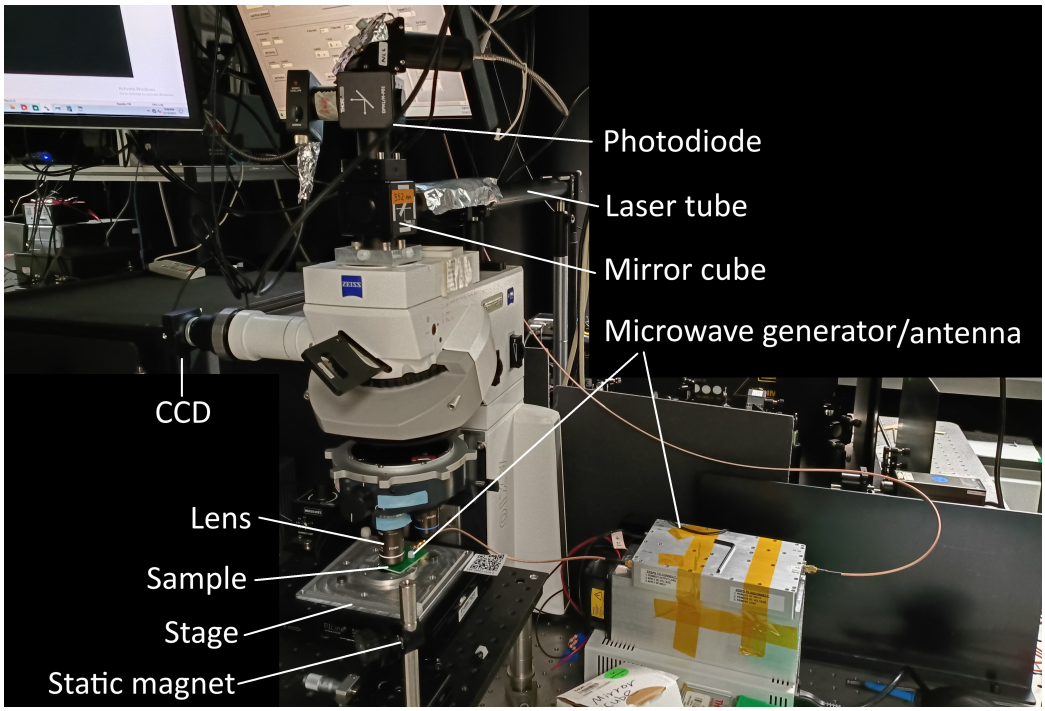

Figure 3.4: *Photograph of the complete experimental setup used for photoluminescence and ODMR measurements. The system is built around a confocal microscope, with optical excitation provided by continuous-wave lasers and microwave delivery achieved via a near-field antenna. Photoluminescence is collected through the same objective and detected using a spectrometer or photodiode depending on the measurement mode.*

Optical excitation was provided by continuous-wave diode lasers at wavelengths of 405 nm and 532 nm. The choice of excitation wavelength allows selective probing of different defect species and optical transitions. Laser power at the sample was controlled manually to balance signal strength against photobleaching and sample heating.

The excitation light was focused onto the sample through a high-numerical-aperture objective, which also collected the emitted photoluminescence. The collected signal was separated from the excitation light using dichroic mirrors and long-pass filters to suppress residual laser scattering. This confocal configuration provides both spatial filtering and enhanced signal-to-background ratio, which is essential for detecting weak emission from individual defects or small ensembles.

Detection was performed using multiple channels depending on the

measurement mode. A spectrometer equipped with a CCD camera cooled to -50 degrees Celsius was used for wavelength-resolved photoluminescence measurements, while a photodiode was employed for time-resolved and intensity-based measurements. Each detector presents different tradeoffs between spectral resolution, temporal resolution, and sensitivity, and was selected accordingly for a given experiment.

Temporal control of the optical excitation was achieved using an acousto-optic modulator (AOM) placed in the laser path. The AOM allows fast switching of the laser intensity by diffracting the incident beam using an acoustically driven refractive index modulation. By controlling the radio-frequency drive signal, the laser beam could be gated on nanosecond to microsecond timescales, enabling pulsed optical excitation synchronized with microwave control sequences.

3.2.2 Microwave delivery and control

Coherent manipulation of the electronic spin states was achieved using microwave excitation resonant with the ground-state spin transitions. Microwaves were generated using a continuous-wave microwave source, with frequency tunable in the GHz range relevant for nitrogen-vacancy centers in diamond. The output of the microwave source was gated using a pulse generator to allow time-domain control of the microwave field for pulsed experiments such as Rabi oscillations.

The microwave signal was subsequently amplified using a broadband microwave amplifier to achieve sufficient driving strength at the sample position. Microwave delivery to the sample was accomplished using a near-field antenna positioned in close proximity to the diamond surface. This configuration enables efficient coupling of the oscillating magnetic field component of the microwave signal to the electronic spin transitions of the color centers, while minimizing power loss.

3.2.3 Integrated ODMR configuration

In addition to the oscillating microwave magnetic field B_1, a static magnetic field B_0 was applied to lift the degeneracy of the spin sublevels. Rather than using a fixed electromagnet, the static field was introduced manually by positioning a small ferromagnet near the sample using a me-

chanical stage. By adjusting the distance between the magnet and the sample, the magnitude of B_0 could be tuned continuously, resulting in a controlled shift of the ODMR resonance frequencies. This method provides a simple and flexible means of applying a static magnetic field without modifying the optical access of the setup.

Microwave radiation was applied simultaneously to drive transitions between the spin sublevels. When the microwave frequency matched the energy splitting between spin states, a redistribution of the spin population occurred, leading to a measurable change in the photoluminescence signal. By sweeping the microwave frequency while monitoring the emitted photoluminescence, spin resonance spectra were obtained.

The presence of the static magnetic field B_0 lifted the degeneracy of the $m_S = \pm 1$ spin states, resulting in multiple resolvable ODMR resonances whose positions depended on the magnitude and orientation of the applied field. The ability to tune B_0 allowed controlled separation of these resonances and facilitated selective addressing of individual spin transitions.

3.3 Measurement protocols and data acquisition

This section describes the experimental protocols used to acquire the optical and spin-resolved data presented in this thesis. The procedures largely follow established methods for photoluminescence spectroscopy, optically detected magnetic resonance, and coherent spin control in solid-state color centers, as described in previous work[22] and instrument manuals.

3.3.1 Photoluminescence spectroscopy

Photoluminescence (PL) spectroscopy was performed to characterize optical emission from defect centers in hexagonal boron nitride and diamond samples. For single-point PL acquisition, the excitation laser was focused onto a fixed position on the sample using the confocal microscope, and the emitted light was collected through the same objective. The collected signal was directed either to a spectrometer for wavelength-resolved measurements.

Measurements were performed using excitation wavelengths of 405 nm and 532 nm in order to probe different excitation pathways and defect species. Emission spectra obtained under different excitation conditions were compared to assess wavelength-dependent changes in the observed photoluminescence features.

3.3.2 ODMR measurements

Optically detected magnetic resonance measurements were performed using a continuous-wave ODMR scheme. During these measurements, the sample was continuously illuminated by the excitation laser while microwave radiation was applied simultaneously. The microwave frequency was swept across the relevant range while monitoring changes in the photoluminescence intensity.

To improve signal-to-noise ratio, lock-in ODMR detection was employed. In this configuration, the microwave amplitude was modulated at a fixed reference frequency, and the resulting modulation of the photoluminescence signal was detected using a lock-in amplifier. This technique suppresses background noise and slow drifts, allowing weak ODMR signals to be resolved more reliably. The modulation frequency and lock-in time constants were chosen in accordance with standard practice and instrument guidelines, as described in the system manuals and previous work.

3.3.3 Coherent control measurements

Coherent spin control was investigated through time-domain microwave excitation, focusing on Rabi oscillation measurements. In these experiments, microwave pulses of variable duration were applied resonantly to the spin transition while the optical excitation was used for initialization and readout. The photoluminescence intensity was recorded as a function of microwave pulse length.

The resulting oscillatory signal reflects coherent population transfer between spin sublevels. The Rabi frequency was extracted from the oscillation period, while the decay envelope of the oscillations was used to estimate the transverse coherence time T_2. These measurements followed standard pulsed ODMR protocols as described in previous studies and instrument documentation.

3.3.4 Spin relaxation T_1 measurement protocol

Although no T_1 relaxation data are presented in this thesis, the corresponding measurement protocol is included for completeness and future reference. The spin relaxation time T_1 is typically measured using an inversion-recovery pulse sequence. In this protocol, the spin population is first inverted using a resonant microwave pulse, followed by a variable waiting time during which relaxation toward thermal equilibrium occurs.

After the waiting period, the spin state is read out optically, and the photoluminescence signal is recorded as a function of the delay time. Fitting the recovery curve yields the longitudinal relaxation time T_1. This method is widely used in solid-state spin systems and provides complementary information to coherence measurements.

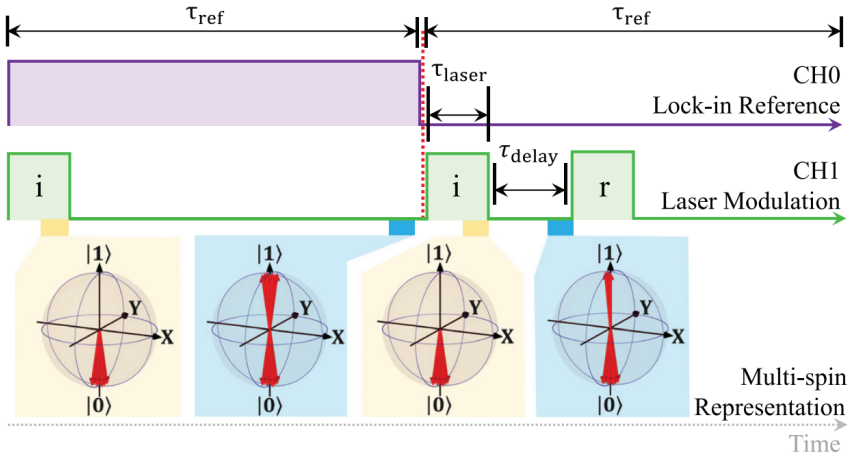

Figure 3.5: *Protocol for extracting the relaxation time T_1 following an inversion-recovery pulse sequence. Image retrieved [21].*

3.4 Data analysis

The experimental data obtained in this work were analyzed using custom scripts written in Python. For photoluminescence measurements, raw spectra were normalized to facilitate comparison between different excitation wavelengths and sample locations. No automated peak identification or fitting was applied at this stage, as the assignment of spectral features is highly sample-dependent and is instead addressed qualitatively in the

Discussion chapter.

For coherent control measurements, Rabi oscillation data were analyzed by fitting an exponentially damped sinusoidal function to the measured photoluminescence signal, as seen in the Theory chapter in 2.4.1. The fitting was performed using the `curve_fit` routine from the `scipy.optimize` module. The decay constant extracted from the exponential envelope was taken as an estimate of the transverse coherence time T_2. The uncertainty associated with the extracted fit parameters was obtained directly from the covariance matrix returned by the fitting routine. The nonlinear least-squares fit was performed using the `scipy.optimize.curve_fit` function, which estimates the covariance matrix $\mathbf{C}$ of the fitted parameters under the assumption of locally linear behavior near the optimum. The standard error σ_{p_i} of a fitted parameter p_i was taken as the square root of the corresponding diagonal element of the covariance matrix,

$$\sigma_{p_i} = \sqrt{C_{ii}}, \tag{3.1}$$

where C_{ii} denotes the i^{th} diagonal element of $\mathbf{C}$. In particular, the uncertainty of the extracted coherence time T_2 was obtained from the diagonal covariance element associated with the exponential decay constant of the fitted Rabi oscillation.

Chapter 4

Results

This chapter presents the experimental results obtained from optical and spin-resonance measurements on two material systems: hexagonal boron nitride and pink diamond. The results are organized into two sections corresponding to these materials. Section 4.1 focuses on photoluminescence measurements of defect centers in hexagonal boron nitride flakes, including representative spectra acquired under different excitation wavelengths and spatially resolved maps of selected flakes. Section 4.2 presents measurements performed on pink diamond, including a photoluminescence spectrum, optically detected magnetic resonance sweeps, and time-domain coherent control measurements in the form of Rabi oscillations. The results are presented in a descriptive manner, with interpretation and comparison to existing literature deferred to the Discussion chapter.

4.1 Hexagonal boron nitride

This section presents the photoluminescence results obtained from hexagonal boron nitride flakes supported on silicon substrates. Measurements were performed on a set of seven individual flakes, each investigated under separate excitation and treatment conditions. Navigation to the flakes was done manually, which rendered finding the exact same placement for the varying conditions impossible. For each flake, spatially resolved photoluminescence maps and corresponding spectra were acquired using an excitation wavelength of 405 nm, both before and after helium ion implantation; and additional spectra were acquired at 532 nm after helium ion implantation as well.

4.1.1 Flake overview

The unnormalized photoluminescence spectra of a grid of 49 uniformly distributed pixels are shown for each flake under varying excitation conditions, as illustrated in Figure 4.1. Presenting spectra from non-selected pixels provides an overview of the emission behavior across the entire flake, rather than focusing only on isolated high-intensity regions. This approach is useful for identifying which wavelength ranges exhibit significant luminescence and therefore informs the choice of wavelengths used for spatially resolved photoluminescence maps. More importantly, the spectra facilitate qualitative comparison between flakes and help guide the selection of regions and spectral features for the sections that follow.

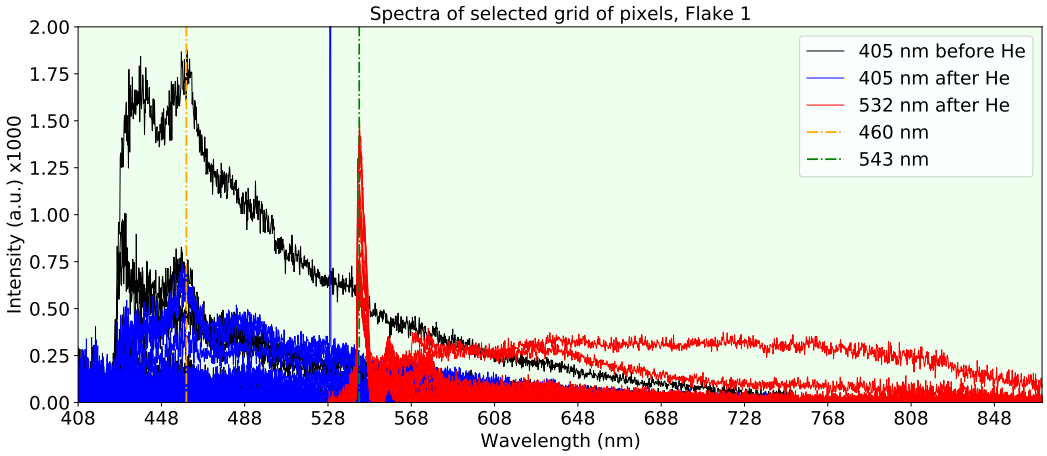

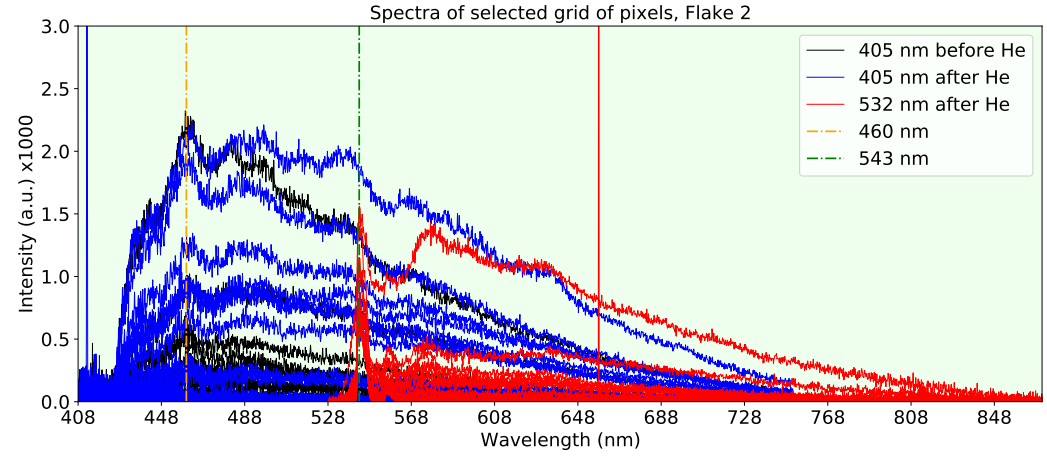

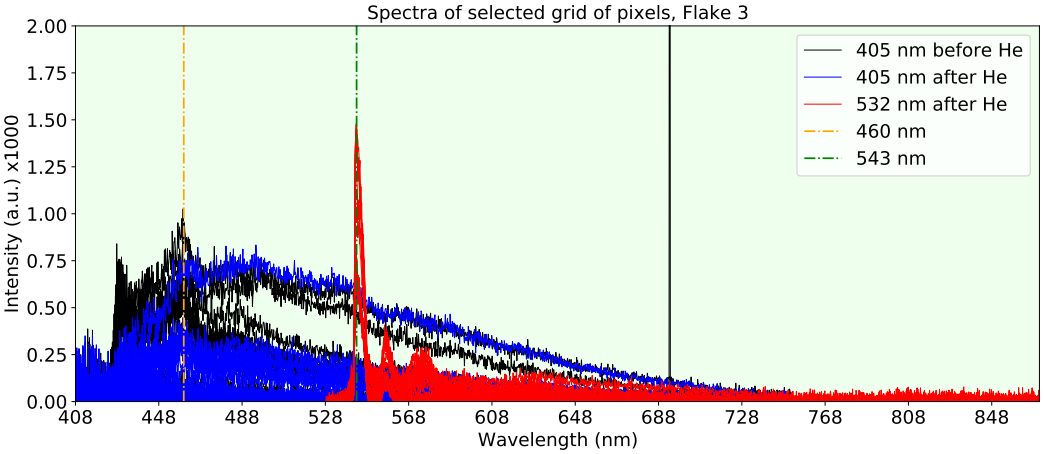
Spectra of selected grid of pixels, Flake 3
Intensity (a.u.) x1000
Wavelength (nm)
405 nm before He
405 nm after He
532 nm after He
460 nm
543 nm

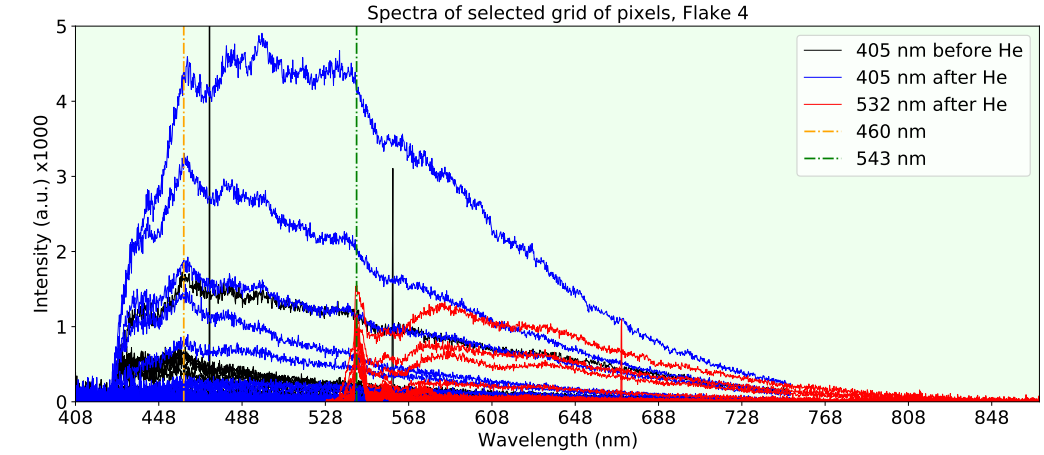
Spectra of selected grid of pixels, Flake 4
Intensity (a.u.) x1000
Wavelength (nm)
405 nm before He
405 nm after He
532 nm after He
460 nm
543 nm

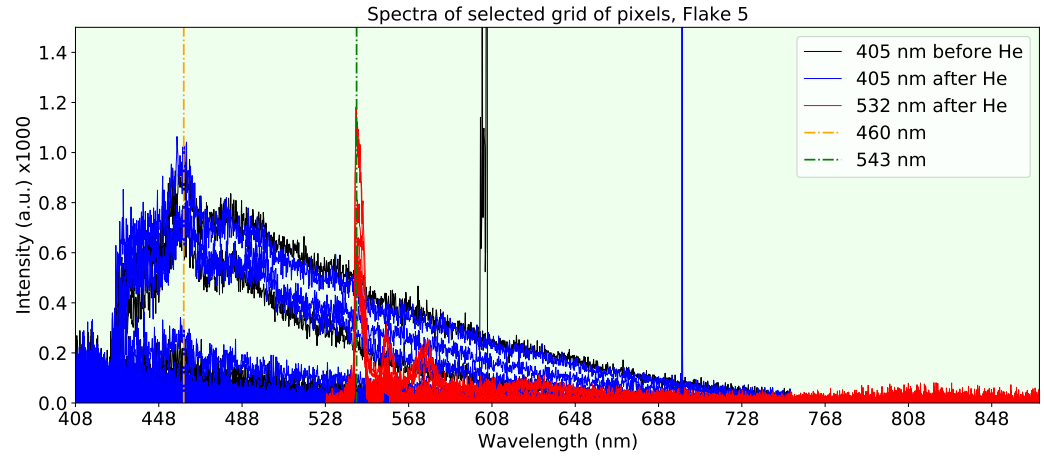
Spectra of selected grid of pixels, Flake 5
Intensity (a.u.) x1000
Wavelength (nm)
405 nm before He
405 nm after He
532 nm after He
460 nm
543 nm

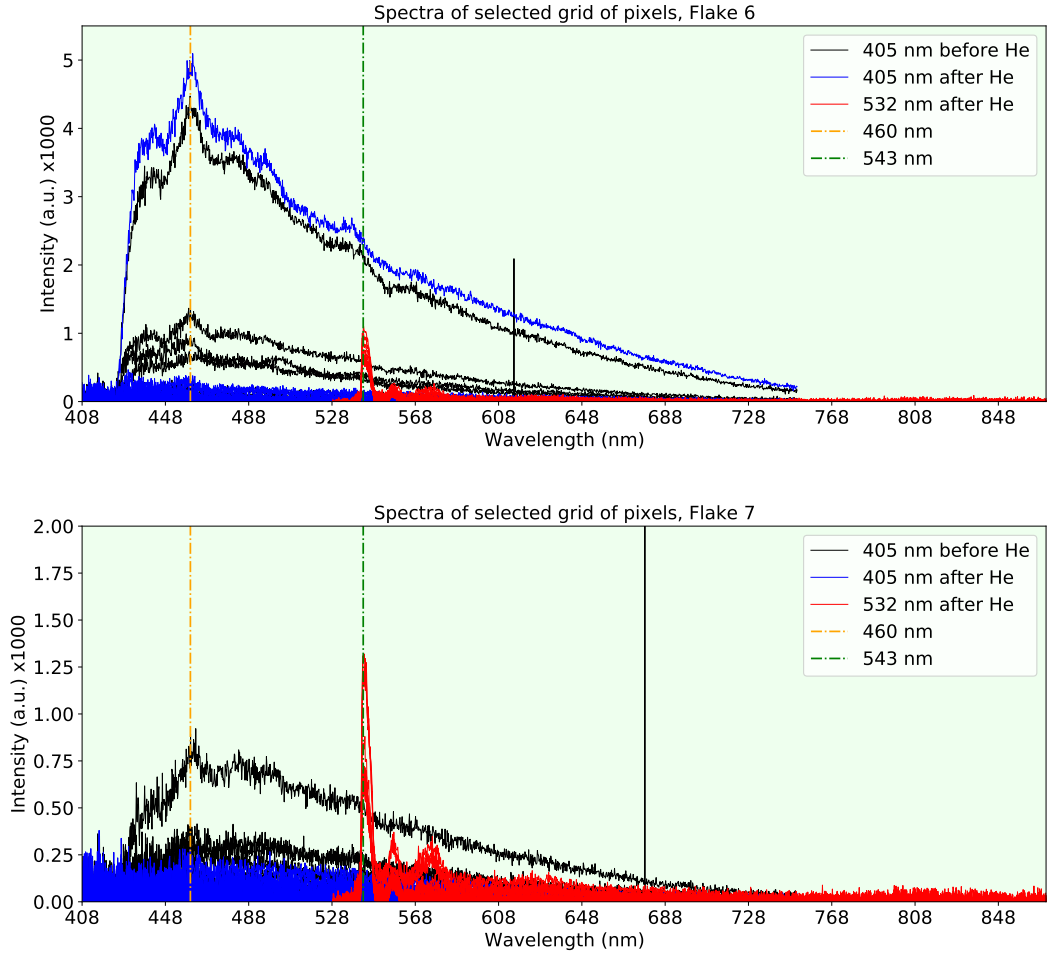

Figure 4.1: *Unnormalized photoluminescence spectra extracted from a grid of 49 uniformly distributed pixels for each of the seven investigated hBN flakes. For each flake, spectra are shown under different excitation conditions, including 405 nm excitation before helium implantation, 405 nm excitation after implantation, and 532 nm excitation after implantation. Vertical dashed lines indicate selected wavelengths of interest used later for spatially resolved photoluminescence mapping.*

To complement the spectral overview in Figure 4.1, spatially resolved photoluminescence maps of six of the seven flakes are shown in Figure 4.2, using the emission maxima found in Figure 4.1 as a basis for optimal imaging.

Figure 4.2 shows merged spatially resolved photoluminescence images of six of the seven investigated hBN flakes under different excitation and

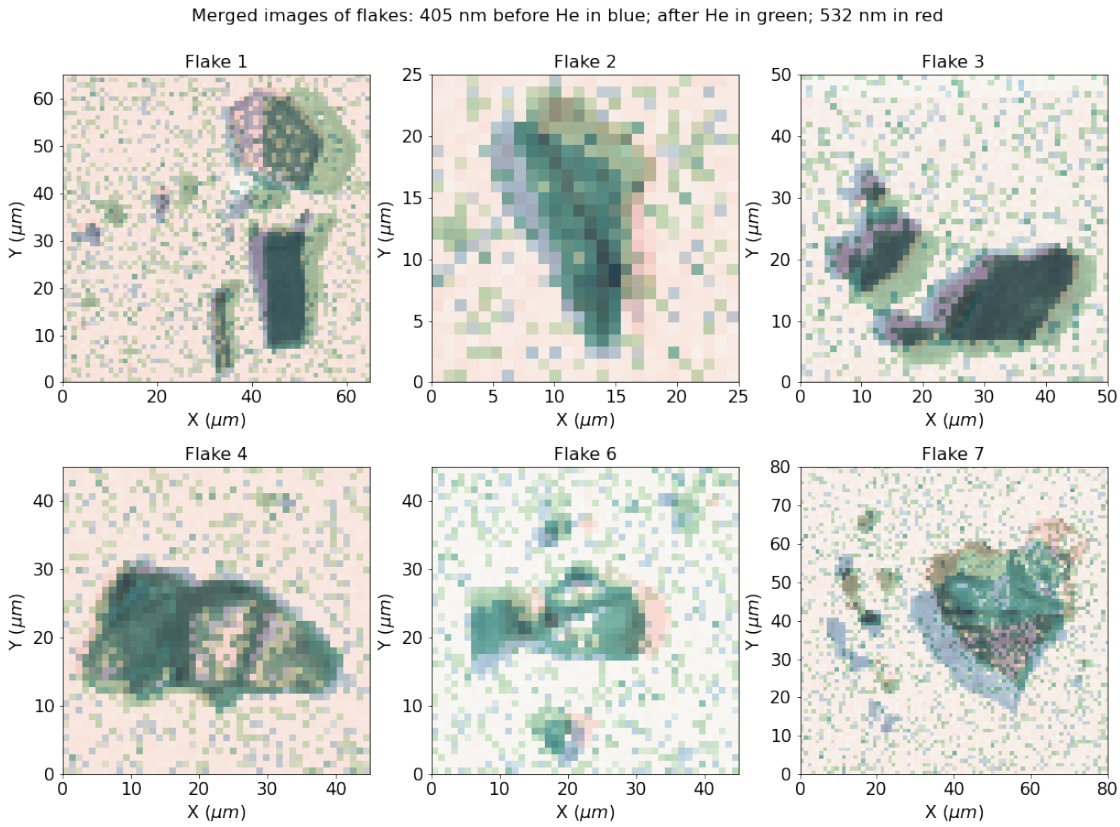

Figure 4.2: *Composite photoluminescence maps of six of the seven hBN flakes, obtained by overlaying spatially resolved emission under different excitation conditions. Emission excited at 405 nm before He implantation is shown in blue, 405 nm after He implantation in green, and 532 nm excitation after He implantation in red. Intensity values are displayed on a logarithmic scale to enhance contrast. The overlays highlight changes in emission intensity and spatial distribution induced by implantation and excitation wavelength. See Appendix for optical images.*

treatment conditions. Flake 5 was omitted due to noise. The apparent spatial offsets between the color channels arise from the fact that the maps were acquired at different times, requiring independent manual realignment of the sample between measurements. As a result, the flake outlines do not perfectly overlap across excitation conditions. Additionally, the mapped regions differ in size between flakes, reflecting variations in the chosen scan area during acquisition and intrinsic differences in flake di-

mensions. The displayed intensities are obtained from the photoluminescence signal via a non-linear transformation, specifically $\log(\max(I, 0))$, in order to enhance contrast across a wide dynamic range. Consequently, relative brightness in the images should be interpreted qualitatively rather than as a direct linear measure of emission intensity.

4.1.2 Photoluminescence comparison

To directly compare the photoluminescence response under different excitation conditions, a region of interest was identified within a flake. Care was taken to select the same spatial area across the three datasets corresponding to excitation at 532 nm before helium implantation, 532 nm after implantation, and 405 nm after implantation. The photoluminescence spectra of all pixels within this region were then summed to obtain an integrated spectrum for each condition. Finally, the three spectra were mean-normalized and plotted together to highlight relative differences in spectral shape and emission features rather than absolute intensity.

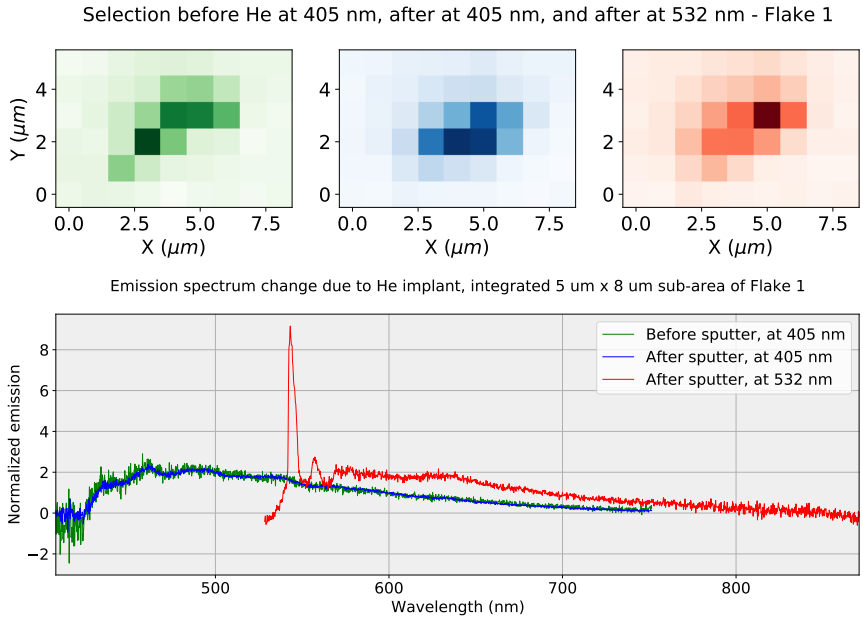

Figure 4.3: *Top: spatial selections of the same sub-region of Flake 1 under three measurement conditions (405 nm excitation before He implantation, 405 nm excitation after He implantation, and 532 nm excitation after He implantation). Bottom: normalized photoluminescence spectra obtained by integrating the emission over the selected 5 μm $\times$ 8 μm area for each condition, illustrating changes in spectral shape with excitation wavelength and implantation.*

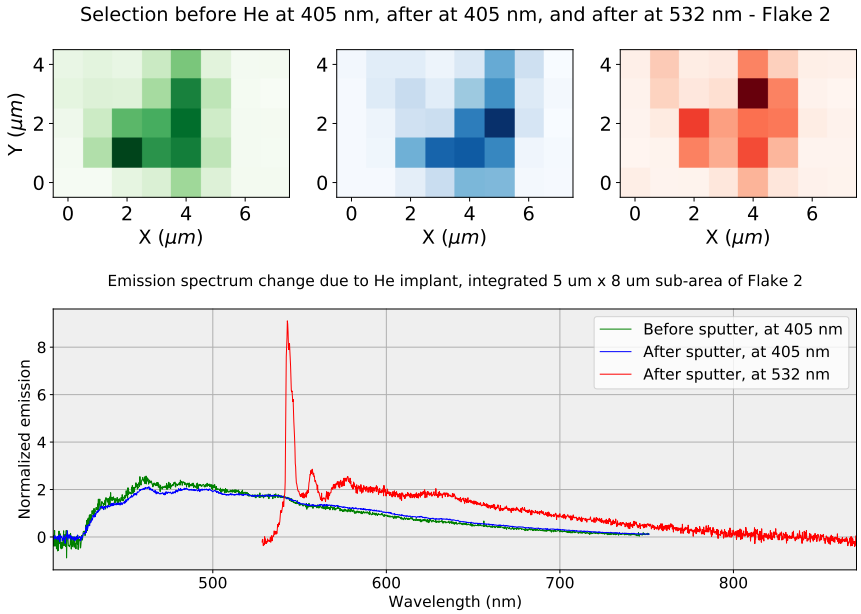

Figure 4.4: *Top: spatial selections of the same sub-region of Flake 2 under three measurement conditions (405 nm excitation before He implantation, 405 nm excitation after He implantation, and 532 nm excitation after He implantation). Bottom: normalized photoluminescence spectra obtained by integrating the emission over the selected* 5 μm $\times$ 8 μm *area for each condition, illustrating changes in spectral shape with excitation wavelength and implantation.*

Figures 4.3 and 4.4 show representative integrated photoluminescence spectra extracted from spatially corresponding regions of selected hBN flakes under different excitation conditions. For all shown cases, the spectra obtained at 405 nm excitation before and after helium implantation exhibit very similar overall shapes and intensities once normalized. The spectra acquired at 532 nm excitation after implantation display a clear qualitative difference relative to the 405 nm measurements. While differences before and after He implantation can be seen in the 405 nm measurements in Figure 4.4, this difference is small, and the shape remains largely unchanged within the measurement sensitivity.

Across all investigated flakes, the qualitative behavior observed in Figures 4.3 and 4.4 was found to be reproducible. In particular, photoluminescence spectra acquired before and after He implantation under identical excitation conditions show no systematic emergence or suppression of distinct emission features. Likewise, for a given flake, changes in excitation wavelength lead to clear differences in the relative spectral weights,

while the overall spectral shape remains broadly similar between flakes. These trends were consistently observed for all flakes studied, suggesting that the effects reported here are representative of the sample set rather than isolated to a single region or flake. It should be noted, however, that the normalization procedure used to compare spectra emphasizes relative spectral shape rather than absolute emission intensity, meaning that changes in overall brightness between excitation conditions may be suppressed.

4.2 Pink diamond

This section presents the experimental results obtained from measurements on the pink diamond sample. In contrast to the hexagonal boron nitride measurements discussed above, the diamond data allow access not only to optical properties, but also to spin-resolved measurements via optically detected magnetic resonance and time-domain microwave control. The results presented here therefore focus on photoluminescence characterization, ODMR spectra under an applied static magnetic field, and coherent spin control as probed through Rabi oscillations.

4.2.1 Photoluminescence

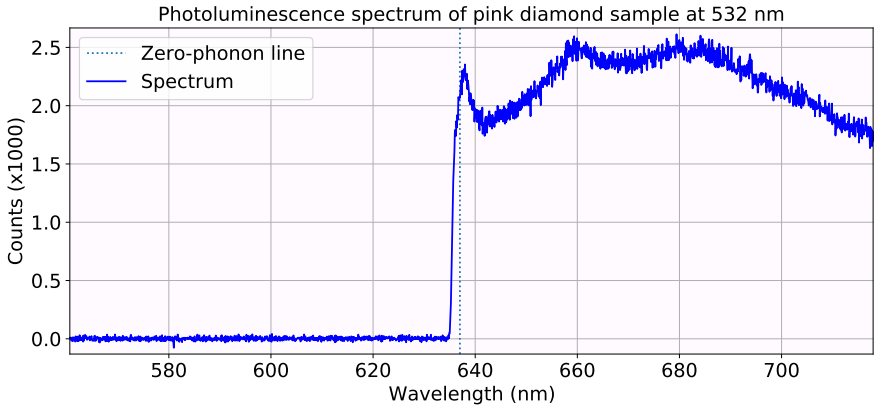

Figure 4.5: *Photoluminescence spectrum of the pink diamond sample under 532 nm excitation.*

Figure 4.5 shows the photoluminescence spectrum of the pink diamond sample under continuous-wave excitation at 532 nm. The spectrum exhibits a broad phonon sideband characteristic of nitrogen-vacancy centers

in diamond, with enhanced emission in the spectral region around the zero-phonon line at approximately 637 nm, characteristic of the negatively charged nitrogen-vacancy (NV^-) center in diamond [8, 17]. The overall spectral shape and intensity are consistent with ensemble emission from NV centers and confirm the optical activity of the sample prior to further spin-resonance measurements.

4.2.2 ODMR

ODMR measurements were performed on the pink diamond sample under continuous optical excitation while sweeping the microwave frequency across the ground-state spin transitions. Figure 4.6 shows ODMR spectra acquired at different microwave attenuation levels. Increasing attenuation leads to a systematic reduction in ODMR contrast, while the resonance frequencies remain unchanged. Based on these measurements, an attenuation of 15 dB was chosen for subsequent experiments, including peak-splitting measurements and all coherent control experiments. This choice is consistent with the operating conditions reported by the previous study on the same sample, which identified similar attenuation levels as a suitable compromise between signal contrast and microwave power broadening [22]. The same study further reported that variations in optical excitation power did not significantly affect ODMR spectra, and laser power was therefore not varied systematically in the present work.

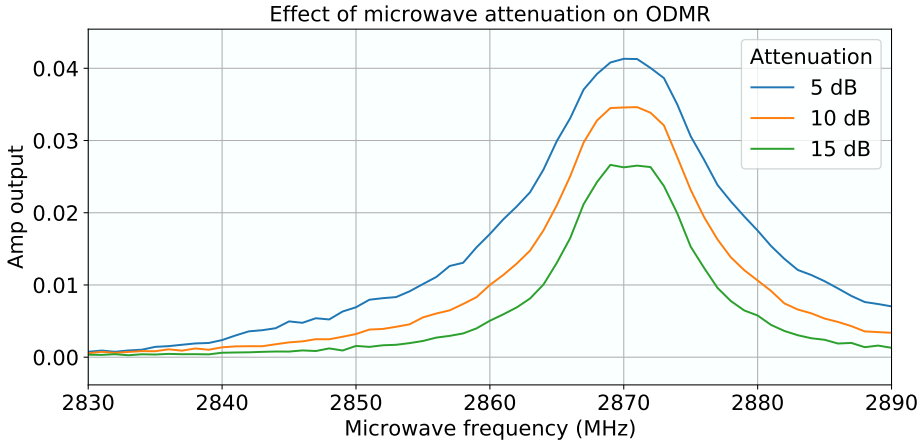

Figure 4.6: *Optically detected magnetic resonance contrast measured at different microwave attenuation levels.*

Figure 4.7 shows ODMR spectra recorded while introducing a static magnetic field B_0 by moving a ferromagnet closer to the sample. As the magnetic field strength increases, the single resonance observed at zero field splits into multiple distinct peaks. At sufficiently large B_0, a total of eight resonances should be resolved; however, only four are visible. Splitting into eight peaks would be consistent with the presence of four crystallographic orientations of the nitrogen-vacancy center in diamond, combined with the lifting of the degeneracy between the $m_S = \pm 1$ spin states under an external magnetic field, as discussed in Chapter 2. Such peak multiplicities were observed in previous work on the same sample [22].

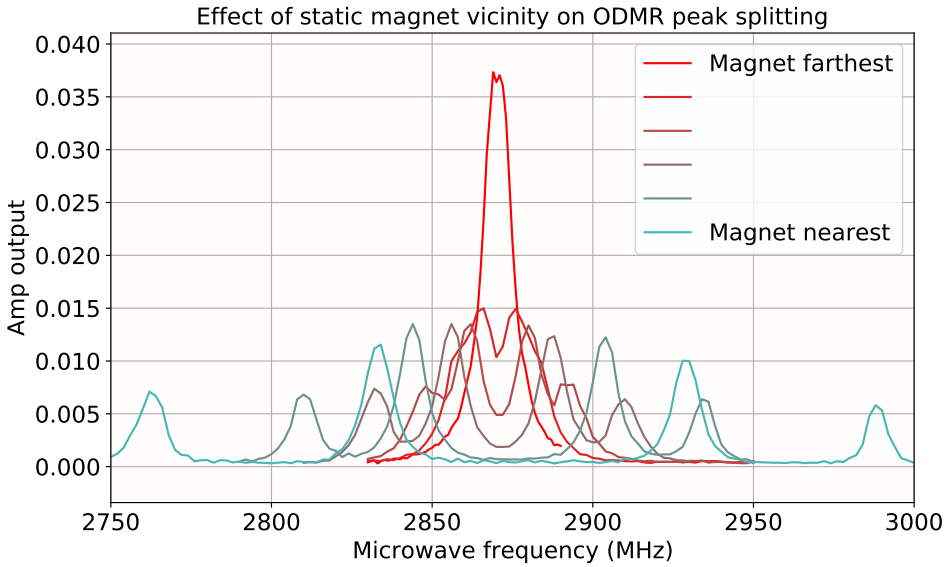

Figure 4.7: *ODMR spectra of the pink diamond measured for different positions of an external permanent magnet. As the static magnetic field B_0 is increased, the resonance peaks split and shift, revealing four distinct peaks, rather than the expected eight.*

4.2.3 Rabi oscillations

Coherent microwave control of the electronic spin states in the pink diamond was investigated using Rabi oscillation measurements. In this protocol, the sample was continuously optically pumped while resonant microwave pulses of varying duration were applied, and the resulting photoluminescence was recorded as a function of pulse length. When the

microwave drive is resonant with a spin transition, the spin population undergoes coherent oscillations between the involved spin states, which manifest as oscillations in the detected photoluminescence intensity.

Figure 4.8 shows a representative Rabi measurement obtained under a static magnetic field B_0, with the microwave power fixed at an attenuation of 15 dB, consistent with the optimization discussed in the previous subsection. The raw photoluminescence data exhibit clear oscillatory behavior with a decaying envelope, indicative of coherent spin manipulation subject to decoherence processes. To guide the eye, a running mean over five points is shown alongside the raw data.

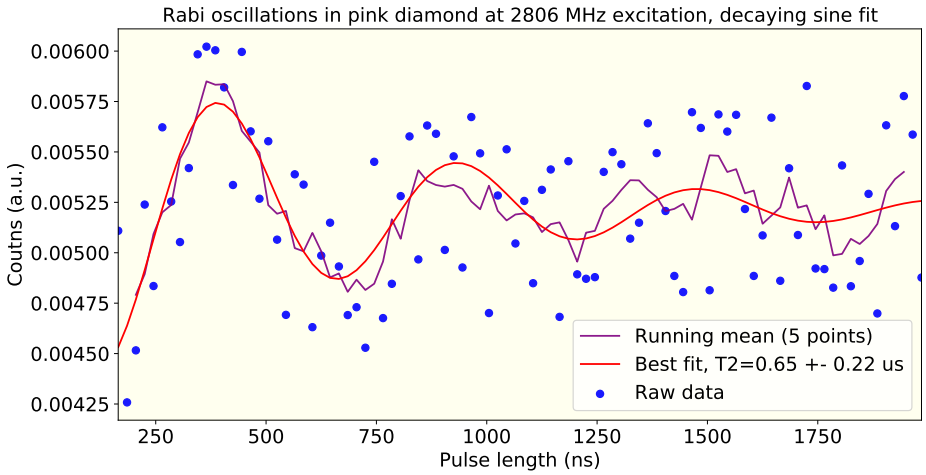

Figure 4.8: *Rabi oscillations measured on the pink diamond NV ensemble under resonant microwave driving. Blue points show the raw photoluminescence signal as a function of microwave pulse duration, the purple line indicates a running mean (5 points), and the red curve is a fit to an exponentially damped sinusoid, from which a coherence time $T_2 = 0.65 \pm 0.22$ μs is extracted.*

The data were fitted using an exponentially damped sinusoidal model,

$$I(t) = A \sin(\Omega_R t + \phi)\, e^{-t/T_2} + C, \tag{4.1}$$

where Ω_R is the Rabi frequency and T_2 is the effective transverse coherence time extracted from the decay envelope. From the fit shown in Figure 4.8, a coherence time of $T_2 = 0.65 \pm 0.22$ μs was obtained. While the uncertainty is relatively large due to noise and limited signal contrast, the result is consistent with the presence of coherent spin control and with previously

reported room-temperature measurements on similar diamond samples, even exceeding the highest T_2 previously achieved, albeit within the error margin [22].

Chapter 5

Discussion

This chapter discusses the experimental results presented in Chapter 4 in the context of existing literature and the theoretical background introduced earlier. The aim is not only to highlight the key observations, but also to critically assess the limitations of the measurements, unresolved questions, and possible explanations for the observed behavior. Where appropriate, results are compared to previous work, in particular the thesis of J. Li, of which this work is a continuation [22].

5.1 Hexagonal boron nitride

The photoluminescence measurements on hexagonal boron nitride flakes reveal a broad and heterogeneous optical response across different flakes, excitation wavelengths, and implantation conditions. While this diversity complicates a direct attribution of specific emission features, it also reflects the rich defect landscape characteristic of hBN.

Across all investigated flakes, photoluminescence spectra exhibit broad emission bands rather than sharp zero-phonon lines, with overall spectral shapes that remain qualitatively similar before and after helium implantation, suggesting that the implantation conditions used here did not induce strong, spectrally distinct new emitters within the sensitivity of the present measurements.

Spatially resolved maps further show that emission intensity is highly non-uniform within individual flakes. Although slight differences between

excitation wavelengths are visible, the dominant emitting regions tend to persist across measurements, indicating that excitation wavelength primarily modulates excitation efficiency rather than activating entirely different defect populations. A key limitation of the present data set is the absence of time-resolved or single-photon measurements, which would be required to conclusively identify individual quantum emitters.

5.1.1 Possible emitters

Based on the observed emission wavelengths and the absence of sharp zero-phonon lines, several defect types previously reported in hBN may contribute to the measured photoluminescence. Table 5.1 summarizes possible emitters consistent with the spectral ranges observed in this work.

Proposed defect	Typical emission range	Reference
V_B^--related defects	800–850 nm	[13]
Carbon-related complexes	580–750 nm	[16]
Oxygen-related defects	600–700 nm	[11]
Unknown deep-level defects	Broad (no clear ZPL)	[15]

Table 5.1: *Possible defect-related emitters in hBN consistent with the observed photoluminescence spectra.*

The broad nature of the measured spectra, combined with the lack of clearly resolved zero-phonon lines, suggests that the emission likely originates from an ensemble of defects rather than isolated single emitters. While helium implantation has been reported to activate or modify defect emission in hBN, the present data do not show a systematic or reproducible spectral signature attributable to implantation alone. This may be due to insufficient implantation dose, post-processing effects, or limitations of the optical setup.

5.2 Pink diamond

The pink diamond measurements focus on optically detected magnetic resonance and coherent spin control of NV centers. Compared to the hBN measurements, the diamond system exhibits clearer and more reproducible spin-dependent optical signatures, consistent with its well-established

defect physics.

Continuous-wave ODMR measurements show clear resonance features that shift systematically with the application of a static magnetic field. Although multiple resonance peaks are observed, their number is fewer than the eight peaks expected from four crystallographic NV orientations combined with spin degeneracy. This discrepancy may arise from preferential optical alignment, or limited sensitivity to certain NV orientations under the chosen experimental conditions. The symmetrical splitting in Figure 4.7 strongly suggests that the spin degeneracy had been lifted.

Microwave power dependence measurements confirm that an attenuation of 15 dB provides a suitable compromise between signal strength and spectral broadening, in agreement with previous work [22]. Laser power was not varied systematically, as previous work demonstrated that it does not significantly affect ODMR contrast within the operating regime used here.

5.2.1 T_2 measurement

Rabi oscillation measurements enable an estimate of the transverse spin coherence time T_2 for the NV centers in the pink diamond. The extracted coherence time is slightly larger than the known value [22], but the associated uncertainty is also comparatively large.

Given the overlap of the error bars, it is not possible to conclusively claim an improvement in coherence time. The apparent increase may instead reflect differences in fitting procedure, signal-to-noise ratio, or experimental stability. Nevertheless, the observation of coherent oscillations and a decay time on the same order of magnitude as previous work confirms the validity of the experimental setup and analysis approach.

5.3 Helium implantation

Helium implantation was intended to modify defect populations in both hBN and diamond samples. While implantation parameters were well defined for the diamond sample, post-implantation photoluminescence measurements did not yield usable spectra. This may be due to experimental

misalignment, surface damage, or excessive non-radiative recombination induced by implantation, though the latter is unlikely.

In the case of hBN, implantation did not result in a clear or reproducible change in the photoluminescence spectra. This outcome highlights the sensitivity of defect engineering in hBN to implantation conditions and post-processing steps, and suggests that further optimization or annealing may be required to reliably activate desired emitters.

5.4 Outlook

Several avenues for future work emerge from this study. For hBN, single-emitter spectroscopy combined with photon correlation measurements would be essential to unambiguously identify defect species. Controlled implantation studies with well-characterized doses and post-implantation annealing could further clarify the role of helium in defect activation.

For diamond, improved magnetic field control using calibrated electromagnets could enable systematic studies of NV orientation-dependent effects. More advanced pulse sequences, such as Hahn echo or dynamical decoupling, would allow more accurate determination of T_2 and separation of different decoherence mechanisms.

Finally, as material science develops at a rapid pace, new exotic materials are being discovered continuously. Coherent control measurements prove to be a great source of extracting knowledge from these new materials; and as a new room-temperature wide-bandgap semiconductor with long spin coherence could already be in the process of being built, it will do no harm to have a foundation for future experiments ready.

Chapter 6

Conclusion

In this thesis, the optical and spin properties of color centers in wide-bandgap semiconductors were investigated using photoluminescence spectroscopy and optically detected magnetic resonance. Two material systems were studied in parallel: hexagonal boron nitride flakes on silicon and a pink diamond containing nitrogen-vacancy centers. The work aimed to assess the suitability of these systems for room-temperature quantum applications and to explore the effects of helium implantation on their optical and spin-related behavior.

For hexagonal boron nitride, spatially resolved photoluminescence measurements revealed a variety of emission features across different flakes and excitation wavelengths. While clear and reproducible changes due to helium implantation were not observed, the measurements provided a systematic overview of the optical response of multiple flakes and highlighted the strong dependence of emission characteristics on excitation conditions and local sample heterogeneity. These results emphasize the challenges associated with defect identification in hBN and motivate further studies with improved control over implantation parameters and post-processing.

In the case of pink diamond, optically detected magnetic resonance measurements confirmed coherent spin control of nitrogen-vacancy centers at room temperature. Rabi oscillations were observed, demonstrating coherent microwave-driven spin dynamics. From an exponentially damped sinusoidal fit to the Rabi data, a transverse spin coherence time of

$$T_2 = (0.65 \pm 0.22)\,\mu\text{s}$$

was extracted. Although the uncertainty is relatively large, this value is consistent with previous measurements on similar samples and validates the experimental setup and analysis methods employed in this work.

Overall, this thesis establishes an experimental and analytical framework for the study of color centers in wide-bandgap semiconductors. While the results are limited by data quality and experimental constraints, they can serve as a foundation for future work involving improved spin control, defect engineering, and the exploration of emerging quantum materials.

Acknowledgments

Foremost, I would like to wholeheartedly thank Dr. Andrew Bettiol for inviting me to the research group, by responding to an e-mail in his spam box, no less. The experience has been truly life-changing and I am deeply grateful for this opportunity.

I would like to thank Dr. Haidong Liang for being my daily supervisor, giving me ideas where necessary and generously helping in various ways, such as implanting helium for me at CIBA.

My sincerest gratitude goes out to Dr. Xingni Chai, who, despite not being assigned to supervise me and being amidst writing her thesis, took her time not only to show me around, but also to teach me how to use the set-up at OMAD and even to gather some data, much of which has been used in this thesis. I'm sorry I wasn't at your ceremony.

My warm thanks to Dr.ir. Bas Hensen, my Leiden supervisor for being available and kindly supporting me.

Thank you to everyone at OMAD, especially Pat and Fred, who made walking into the lab more enjoyable.

My utmost gratitude goes out to Dr. Chara Papathanasiou, my study advisor, who went through mountains of paperwork while also always steering me in the right direction. I appreciate it.

Thanks to the Leiden University Fund for their monetary support.

Thanks to the Erasmus+ International Credit Mobility program making such exchanges possible.

Bibliography

[1] M. A. Nielsen and I. L. Chuang, *Quantum Computation and Quantum Information*, Cambridge University Press, Cambridge (2000).

[2] J. P. Dowling and G. J. Milburn, "Quantum technology: the second quantum revolution," *Philosophical Transactions of the Royal Society A* **361**, 1655–1674 (2003).

[3] M. H. Devoret and R. J. Schoelkopf, "Superconducting circuits for quantum information: an outlook," *Science* **339**, 1169–1174 (2013).

[4] P. Krantz, M. Kjaergaard, F. Yan, T. P. Orlando, S. Gustavsson, and W. D. Oliver, "A quantum engineer's guide to superconducting qubits," *Applied Physics Reviews* **6**, 021318 (2019).

[5] I. Aharonovich and E. Neu, "Diamond nanophotonics," *Advanced Optical Materials* **2**, 911–928 (2014).

[6] D. D. Awschalom, R. Hanson, J. Wrachtrup, and B. B. Zhou, "Quantum technologies with optically interfaced solid-state spins," *Nature Photonics* **12**, 516–527 (2018).

[7] C. L. Degen, F. Reinhard, and P. Cappellaro, "Quantum sensing," *Reviews of Modern Physics* **89**, 035002 (2017).

[8] M. W. Doherty, N. B. Manson, P. Delaney, F. Jelezko, J. Wrachtrup, and L. C. L. Hollenberg, "The nitrogen-vacancy color center in diamond," *Physics Reports* **528**, 1–45 (2013).

[9] J. R. Weber *et al.*, "Quantum computing with defects," *Proceedings of the National Academy of Sciences* **107**, 8513–8518 (2010).

[10] W. F. Koehl, B. B. Buckley, F. J. Heremans, G. Calusine, and D. D. Awschalom, "Room temperature coherent control of defect spin qubits in silicon carbide," *Nature* **479**, 84–87 (2011).

[11] T. T. Tran *et al.*, "Quantum emission from hexagonal boron nitride monolayers," *Nature Nanotechnology* **11**, 37–41 (2016).

[12] A. Çakan, C. Cholsuk, A. Gale, M. Kianinia, S. Paçal, S. Ateş, I. Aharonovich, M. Toth, and T. Vogl, "Quantum optics applications of hexagonal boron nitride defects," *Advanced Optical Materials* **13**, 2402508 (2025).

[13] A. Gottscholl, M. Kianinia, V. Soltamov, S. Orlinskii, G. Mamin, C. Bradac, C. Kasper, K. Krambrock, A. Sperlich, M. Toth, I. Aharonovich, and V. Dyakonov, "Initialization and read-out of intrinsic spin defects in a van der Waals crystal at room temperature," *Nature Materials* **19**, 540–545 (2020).

[14] G. Grosso, H. Moon, B. Lienhard, S. Ali, D. K. Efetov, M. M. Furchi, M. J. Ford, I. Aharonovich, and D. Englund, "Tunable and high-purity room temperature single-photon emission from atomic defects in hexagonal boron nitride," *Nature Communications* **8**, 705 (2017).

[15] C. Fournier, A. Plaud, S. Roux, A. Pierret, M. Rosticher, K. Watanabe, T. Taniguchi, S. Buil, X. Quélin, J. Barjon, J. Hermier, and A. Delteil, "Position-controlled quantum emitters with reproducible emission wavelength in hexagonal boron nitride," *Nature Communications* **12**, 3779 (2021).

[16] N. Mendelson *et al.*, "Identifying carbon as the source of visible single-photon emission from hexagonal boron nitride," *Nature Materials* **20**, 321–328 (2021).

[17] F. Jelezko and J. Wrachtrup, "Read-out of single spins by optical spectroscopy," *Journal of Physics: Condensed Matter* **16**, R1089–R1104 (2004).

[18] G. Di Maria, "Wide Bandgap (WBG) Semiconductors," *Power Electronics News* (2024). Retrieved from `https://www.powerelectronicsnews.com/wide-bandgap-wbg-semiconductors/`

[19] L. M. Pham *et al.*, "Enhanced metrology using preferential orientation of nitrogen-vacancy centers in diamond," *Physical Review. B, Condensed matter* **86**, 12 (2012).

[20] V. K. Sekwani *et al.*, "Coherent control of NV- centers in diamond in a quantum teaching lab," *American Journal of Physics* **88**, 12 (2020).

[21] A. Khalid *et al.*, "Lifetime Reduction and Enhanced Emission of Single Photon Color Centers in Nanodiamond via Surrounding Refractive Index Modification," *Scientific Reports* **5(1)**:11179 (2015).

[22] J. Li, "Coherent Control of Spin in Color Centers of Wide Bandgap Semiconductors," *MSc Thesis* (2025).

Appendix: Optical hBN flakes 100x